Thermodynamic temperature of the triple point of xenon measured by refractive index gas thermometry

P M C Rourke

National Research Council, 1200 Montreal Road, Ottawa, ON, K1A 0R6, Canada

E-mail: patrick.rourke@nrc-cnrc.gc.ca

CrossMark

Abstract

Measurements of the refractive indices of helium and argon using a quasi-spherical microwave resonator and upgraded experimental protocol are reported at the temperatures of the triple points of water and xenon. The results at the triple point of water are used to determine the compressibility of the resonating cavity, which is bounded by the copper shell of the resonator. This experimentally-determined compressibility is consistent with the literature value for copper, but with much smaller measurement uncertainty. The measured compressibility is extrapolated to the triple point of xenon, and combined with the refractive index results at that temperature to determine the thermodynamic accuracy of the International Temperature Scale of 1990 (ITS-90): $(T - T_{90}) = (-6.9 \pm 1.7)$ mK at ITS-90 temperature $T_{90} = 161.405\,96$ K, corresponding to a xenon triple point thermodynamic temperature of $T = (161.3991 \pm 0.0017)$ K. The experimental compressibility is further extrapolated to the triple points of argon, oxygen and neon, and used to re-analyze earlier refractive index gas thermometry measurements made using the same resonator, yielding updated values with reduced uncertainties: $(T - T_{90}) = (-4.1 \pm 1.6)$ mK at $T_{90} = 83.8058$ K, $(T - T_{90}) = (-2.0 \pm 0.8)$ mK at $T_{90} = 54.3584$ K, and $(T - T_{90}) = (-0.61 \pm 0.49)$ mK at $T_{90} = 24.5561$ K. The ITS-90 thermodynamic accuracy results of the present refractive index gas thermometry study agree with those previously reported by acoustic gas thermometry and dielectric constant gas thermometry.

Keywords: primary thermometry, thermodynamic temperature, refractive index, microwave resonator, xenon, ITS-90

(Some figures may appear in colour only in the online journal)

1. Introduction

1.1. International temperature scale of 1990

The practical temperature scale used as the basis for nearly all thermometer calibrations presently performed worldwide is the International Temperature Scale of 1990 (ITS-90), which approximates true thermodynamic temperature T by scale temperature T_{90} [1, 2]. This scale was formulated based on the best thermodynamic temperature data available at the time of its creation, predominantly from measurements made using the primary thermometry technique of constant-volume gas thermometry (CVGT) [3].

However, since 1990 the refinement of new advanced primary thermometry techniques, such as acoustic gas thermometry (AGT) [4], dielectric constant gas thermometry (DCGT) [5] and refractive index gas thermometry (RIGT) [6], has begun to reveal systematic differences between T_{90} and T: T_{90} deviates from T by more than 3 mK from roughly 75 K to 225 K, and for all temperatures above 295 K [7–14]. Further work is now underway to determine $(T - T_{90})$ as accurately as possible, using multiple experimental techniques to reduce

the potential influence on the overall data set of unmodelled systematic effects intrinsic to any one primary thermometry method. The fruits of this effort may enable the formulation of a new scale with much better thermodynamic accuracy than ITS-90 [15, 16], while simultaneously advancing technical development of modern primary thermometry techniques to facilitate direct dissemination of T [17] according to the new definition of the kelvin [18–20].

Realization of the triple point of mercury (TPHg) at $T_{90} = 234.3156$ K is required for thermometer calibration on the ITS-90 in any subrange that extends below the triple point of water (TPW) at $T_{90} = T = 273.16$ K, but increasingly stringent restrictions on the mining, transport and use of mercury [21] have motivated the thermometry community to search for suitable alternatives. The triple point of xenon (TPXe) at $T_{90} = 161.40596$ K [22] is one of the leading alternative candidates to TPHg, since its placement nearly halfway between TPW and the next closest defining fixed point, the triple point of argon (TPAr) at $T_{90} = 83.8058$ K, improves thermometer interpolation characteristics compared to when TPHg is used in the ITS-90 [23]. TPXe is also located near the point of worst ITS-90 thermodynamic accuracy below TPW [8], so the present work focuses on using RIGT to determine the thermodynamic temperature of TPXe and corroborate $(T - T_{90})$ measurements made by other primary thermometry techniques in this vicinity.

1.2. Refractive index gas thermometry

RIGT is a type of polarizing gas thermometry (PGT) that uses measurements of the refractive index n and pressure p of a working gas to determine the thermodynamic temperature of the gas. At a given (p, T) thermodynamic state, the refractive index of a gas may be calculated as [6]

$$n = \sqrt{\epsilon_r \mu_r}, \qquad (1)$$

by combining virial expansions of the relative dielectric permittivity ϵ_r, relative magnetic permeability μ_r and pressure p, formulated in terms of the molar gas density ρ:

$$\frac{\epsilon_r - 1}{\epsilon_r + 2} = A_\epsilon \rho + B_\epsilon \rho^2 + C_\epsilon \rho^3 + \dots, \qquad (2)$$

$$\frac{\mu_r - 1}{\mu_r + 2} = A_\mu \rho + \dots, \qquad (3)$$

$$p = RT\rho \left[1 + B_\rho \rho + C_\rho \rho^2 + D_\rho \rho^3 + \dots \right], \qquad (4)$$

wherein A_ϵ and A_μ are the molar electric and magnetic polarizabilities of the gas in the $\rho \to 0$ limit; $R = N_A k$ is the molar gas constant, $N_A \equiv 6.02214076 \times 10^{23}$ mol^{-1} is the Avogadro constant, and $k \equiv 1.380649 \times 10^{-23}$ J K^{-1} is the Boltzmann constant [18, 19]; and B_ϵ, C_ϵ, ... and B_ρ, C_ρ, D_ρ, ... are respectively the higher order dielectric and density virial coefficients of the gas.

In general, a hollow conducting cavity resonator will support electromagnetic resonance modes whose resonant
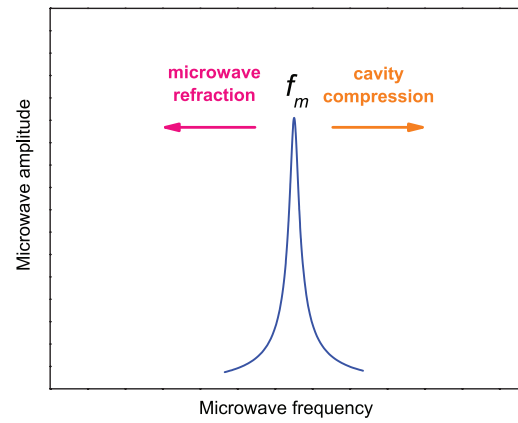

Figure 1. The influence of microwave refraction and cavity compression on a resonant frequency f_m as working gas pressure p increases at constant T.

frequencies $f_m(p, T)$ are related to the refractive index n of the working gas inside the resonator at thermodynamic temperature T and pressure p as [6]

$$f_m(p, T) = \frac{f_m(0, T)}{n \left[1 - \kappa_{\mathrm{eff}} p \right]}, \qquad (5)$$

where m indexes each particular resonance mode and κ_{eff} is the effective compressibility of the cavity. For typical resonating cavities with dimensions on the order of several centimetres, the lowest order resonance modes have frequencies in the GHz range. Compared to vacuum measurements at $p = 0$, where $n \equiv 1$, equation (5) and figure 1 show two competing effects on the resonant frequency f_m of mode m as p is increased at constant T:

(i) Increasing density of the working gas causes n to increase, which causes f_m to decrease.
(ii) Increasing force exerted on the inside and outside of the resonator shell material causes the resonating cavity to shrink, as manifested in the $[1 - \kappa_{\mathrm{eff}} p]$ term, which causes f_m to increase.

If equation (5) is applied at a thermodynamic state with known n and p, experimental resonant frequency measurements can be used to determine κ_{eff}. Conversely, if equation (5) is applied with known values of κ_{eff} and p, experimental resonant frequency measurements can be used to determine n, and therefore T. The degree to which the refractivity and compressibility effects can be characterized, relative to each other and relative to other experimental and theoretical considerations, ultimately dictates the accuracy of a given RIGT experiment.

As with earlier NRC RIGT work, the present study uses a quasi-spherical resonator (QSR) with a 'racetrack' design, constructed of oxygen-free high-conductivity (OFHC) copper [12, 24, 25], which lifts the degeneracy of each resonant mode m to produce a triplet of three individually-resolvable microwave peaks. In this case, equation (5) can be re-written, including geometrical corrections, to express the experimentally-determined refractive index of the working gas as [12, 24–26]

$$n = \frac{c_0}{2\pi \langle f + g \rangle_m} \frac{\langle \xi_{\mathrm{corr}} \rangle_m}{a_{0,m} \left(1 - \frac{\kappa_{\mathrm{T}} p}{3} \right)}, \qquad (6)$$

where c_0 is the speed of light in vacuum; $\langle f + g \rangle_m$ is the average half-width-corrected frequency, which accounts for the penetration of the electromagnetic field into the cavity wall, of triplet m measured at pressure p and temperature T; $a_{0,m}$ is the equivalent radius of a spherical resonator with the same volume as the measured QSR, determined in vacuum at temperature T using triplet m and equation (6) with $n \equiv 1$; $\kappa_{\mathrm{T}} = 3\kappa_{\mathrm{eff}}$ is the isothermal volumetric compressibility of the resonator shell material, and $\langle \xi_{\mathrm{corr}} \rangle_m$ is the average corrected microwave eigenvalue for mode m at pressure p and temperature T [12, 25].

1.3. Resonator compressibility

The isothermal compressibility κ_{T} of a solid material at a given ITS-90 temperature T_{90}^* can be expressed in terms of other properties of the solid as

$$
\begin{aligned}
\kappa_{\mathrm{T}} &= \kappa_{\mathrm{S}} + \Delta_{\mathrm{S} \to \mathrm{T}} \\
&= \frac{1}{B_{\mathrm{S}}(T_{90}^*)} \\
&\quad + \frac{9 \, \alpha_{\mathrm{L}}^2(T_{90}^*) \, T_{90}^*}{\rho_{\mathrm{solid}}(293 \, \mathrm{K}) \, c_{\mathrm{p}}(T_{90}^*)} \left[\int_{T_{90}=293 \, \mathrm{K}}^{T_{90}=T_{90}^*} \alpha_{\mathrm{L}}(T_{90}) \mathrm{d}T_{90} + 1 \right]^3,
\end{aligned}
$$
$$\qquad (7)$$

where κ_{S} is the adiabatic compressibility, $\Delta_{\mathrm{S} \to \mathrm{T}}$ is the conversion factor from adiabatic to isothermal compressibility, B_{S} is the adiabatic bulk modulus, α_{L} is the linear thermal expansion coefficient, c_{p} is the constant-pressure specific heat capacity, and $\rho_{\mathrm{solid}}(293 \, \mathrm{K})$ is the density at $T_{90} = 293$ K (with the subscript 'solid' added to distinguish it from the density of the working gas ρ).

In previous RIGT work at the National Research Council Canada (NRC), κ_{T} was calculated from literature sources for OFHC copper, with the uncertainty in κ_{T}, itself dominated by the uncertainty ascribed to the literature value of B_{S}, contributing the largest uncertainty component on the measured thermodynamic temperature T [12]. This uncertainty component on T increases as T^2 [12], and would reach approximately 9 mK at TPXe. However, the uncertainty in the compressibility may be reduced by directly measuring the resonating cavity compressibility *in situ* using microwave resonance measurements at TPW, where T and therefore n are known, and then extrapolating the measured compressibility to the temperature of interest [6, 27]. The extrapolation from TPW to a given temperature T_{90}^* may be performed via an equation such as

$$\kappa_{\mathrm{S}}(T_{90}^*) = \kappa_{\mathrm{S}}(\mathrm{TPW}) \left[\int_{\mathrm{TPW}}^{T_{90}=T_{90}^*} \alpha_{\mathrm{L}}(T_{90}) \mathrm{d}T_{90} \right]^{3\delta} \qquad (8)$$

where δ is the Anderson–Grüneisen parameter [27].

Furthermore, the sensitivity of the uncertainty in T to the uncertainty in κ_{T} may be reduced by using a more polarizable working gas: for a given (p, T) thermodynamic state, this

will accentuate the resonant frequency shift due to microwave refraction compared to the shift due to cavity compression (see equation (5) and figure 1) [6]. Helium is traditionally used as the RIGT working gas, due to the superiority of *ab initio* calculations of its static polarizability and virial coefficients, but its polarizability is low. On the other hand, argon is $8\times$ more polarizable than helium. While a previous attempt to use argon as a RIGT working gas suffered from large uncertainties in the published physical properties of this gas [13], argon has recently benefited from low-uncertainty experimental determinations of A_ϵ, B_ρ and C_ρ by DCGT [28, 29].

1.4. Article outline

The work presented here is organized as follows: section 2 describes the details of the experimental apparatus, measurement protocol and data analysis techniques, particularly where these differ from the previous NRC RIGT study [12]; section 3 contains the measurements, analysis and uncertainty budget associated with the experimental determination of the resonator compressibility at TPW using helium and argon as working gases; section 4 presents the compressibility extrapolation to lower temperatures, including uncertainty budget; section 5 contains the measurements, analysis and uncertainty budget associated with the experimental determination of $(T - T_{90})$ at TPXe, using the extrapolated compressibility and helium and argon as working gases; previous NRC RIGT $(T - T_{90})$ results and uncertainties using helium as a working gas at the triple point of argon (TPAr) at $T_{90} = 83.8058$ K, the triple point of oxygen (TPO$_2$) at $T_{90} = 54.3584$ K, and the triple point of neon (TPNe) at $T_{90} = 24.5561$ K [12] are re-calculated in section 6 using the measured compressibility from section 3, extrapolated as per section 4; and finally, section 7 summarizes the overall results of the present study and compares them to measurements made with other primary thermometry techniques. All uncertainties are expressed as standard (not expanded) uncertainties.

2. Experimental details

The present study builds on previous RIGT work at NRC, and as such shares many experimental details with earlier publications [12, 25]. In the interest of brevity, this section focuses on the significant upgrades that are unique to the present work.

2.1. T_{90} measurement and control

As shown in figure 2, two new capsule thermometer mounts have been attached to the outside of the resonator, one each on the north and south hemispheres respectively, in order to characterize thermal gradients across the resonator shell. The capsule standard platinum resistance thermometer (CSPRT) with serial number R4794 has been moved from the old thermometry disc to the new thermometer mount on the resonator south hemisphere. A second CSPRT, Leeds and Northrup serial number 1876687, has been added to the new thermometer mount on the resonator north hemisphere. CSPRT 1876687
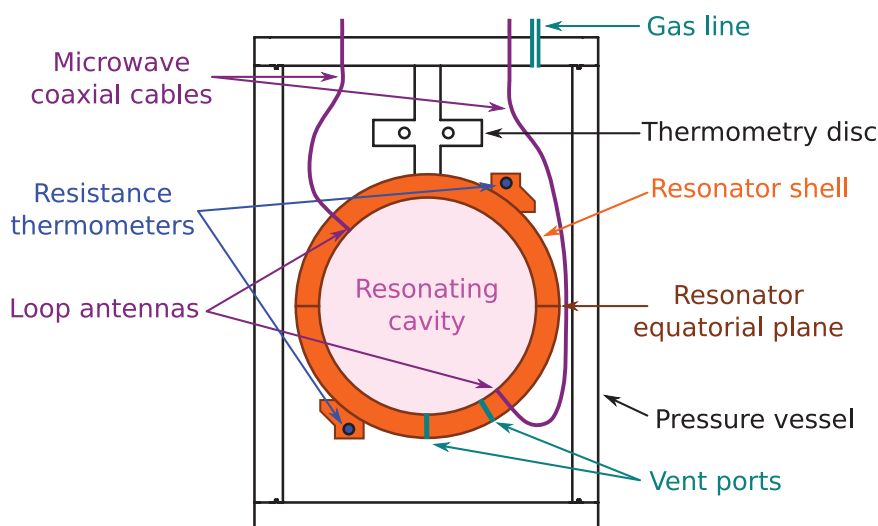
Figure 2. Diagram of RIGT pressure vessel and resonator at NRC, showing new resistance thermometer locations.

was calibrated at NRC in 2015 at the same time as CSPRT R4794, on the ITS-90 subrange spanning from the triple point of equilibrium hydrogen at $T_{90} = 13.8033$ K to TPW, and was also previously used in NRC T_{90} determinations of TPXe [22] and the triple point of sulfur hexafluoride [30]. Both CSPRTs are measured in parallel, by using two dedicated Automatic Systems Laboratories F18 resistance bridges. All T_{90} measurements reported in the present study represent the average over the two thermometers, after correcting the readings of each thermometer for self-heating effects.

The resistive wire heater wrapped around the circumference of the pressure vessel lid, that had previously caused thermal gradients [12], is no longer used; it is replaced in the T_{90} control loop by the resistive cartridge heater mounted on cooling stage 2 of the cryocooler (as per the viability test of the new arrangement described in section 4.2 of [12]).

2.2. Gas pressure p sourcing, filtering, measurement and control

99.9999% pure helium working gas is sourced from a Praxair 6.0 Research Chromatographic grade cylinder (Cylinder No. 1564559Y, from Product Batch No. 303449055503), a newer cylinder than was used in [12]. For the first time in NRC RIGT, 99.9999% pure argon is also used as a working gas, sourced from a Praxair 6.0 Research grade cylinder (Cylinder No. 57022, from Product Batch No. 70319-6292-41). Since the SAES MC1-902 gas purifier from the previous study cannot filter out N_2 or CH_4 impurities, an SAES PS2-GC50 heated getter purifier for rare gas is now used in series with the MC1-902. The new gas purifier removes N_2, O_2, H_2O, CH_4, CO_2, CO and H_2 to <10 parts per billion (ppb) [31]. Neither gas purifier can remove noble gas impurities, and these are not listed on the manufacturer's gas analysis reports (with the exception of argon impurities in the helium cylinder); however, no noble gas impurities were detected in samples of the working gases analyzed by the Finnigan MAT 271 mass spectrometer at the Korea Research Institute of Standards and

Science (KRISS), subject to applicable detection limits. Gas analysis results combined from the KRISS and manufacturer-provided assays are shown in table 1. For argon impurities in helium, the manufacturer's detection limit (0.1 µmol mol^{-1}) is lower than that of KRISS (0.5 µmol mol^{-1}), so the former is listed in table 1.

The data reported herein using helium as the working gas were collected in February–March 2018, whereas those using argon as the working gas were collected in April–May 2018. In order to avoid cross-contamination when switching working gases, the gas-handling system, cryostat gas line, pressure vessel and resonator were turbopumped for one week, then cycle purged three times between vacuum and 700 kPa argon, then turbopumped for one additional week before commencing measurements using argon as the working gas. The gas samples sent to KRISS for noble gas analysis were drawn directly from the pressure vessel working gas used for the RIGT measurements, so table 1 shows that any residual helium in the system at the time of the argon working gas RIGT measurements was below the KRISS detection limit for helium in argon (3.9 µmol mol^{-1}).

In order to avoid the pressure transducer zero offset drift problem seen in the previous study [12], the piston of the Ruska 2465-754 pressure balance is now directly floated to realize p during all microwave measurements performed when working gas is present in the pressure vessel, with the downstream piezoelectric gas flow valve actively controlled by a PID loop to maintain the piston float height. Since the present study focuses on a temperature range approximately 2–3× higher than the highest temperature explored in the previous NRC work, and gas density at a given pressure decreases with increasing temperature, degradation of the strength of the microwave refraction signal has been avoided by upgrading to a Ruska 2465–727 piston/cylinder set (serial number C685), thereby increasing the maximum operating pressure from 200 kPa to 700 kPa. The effective area of the piston was calibrated at the US National Institute of Standards and Technology (NIST) in 2016, with a pressure-dependent

Table 1. Impurity content of working gases.

Impurity species	Concentration in helium gas (μmol mol^{-1})	Concentration in argon gas (μmol mol^{-1})	Removed by gas purifiers?
He	balance	<3.9[a]	No
Ne	<2.4[a]	<24[a,b]	No
Ar	<0.1[c]	balance	No
Kr	<0.6[a]	<0.6[a]	No
Xe	<0.8[a]	<0.8[a]	No
N_2	0.15[c]	0.35[c]	Yes
O_2	<0.1[c]	0.18[c]	Yes
H_2O	<0.2[c]	0.25[c]	Yes
Total hydrocarbons	<0.1[c]	0.02[c]	Yes
CO_2	<0.1[c]	<0.1[c]	Yes
CO	<0.1[c]	<0.1[c]	Yes
H_2	<0.1[c]	—[d]	Yes

[a] KRISS analysis report.
[b] Detection limit for neon in argon increased due to overlapping Ne-20 and Ar ++ mass spectrometer peaks.
[c] Manufacturer's analysis report.
[d] Species not listed in analysis report.

value of $8.402\,142 \times 10^{-5} \left(1 + 1.479 \times 10^{-11}p\right)$ m^2 (where p is expressed in Pa), and pressure-dependent relative standard uncertainty ranging from 5 ppm to 6 ppm. Here relative uncertainties expressed as parts in 10^6 or parts per million are expressed as 'ppm.'

Aside from the specific improvements listed above, the gas-handling system, cryostat gas line geometry and static (non-flowing) gas configuration of the pressure vessel are the same in the present work as in the previous NRC RIGT study [12].

2.3. Measurement protocol

For each working gas and T_{90} set point combination, microwave measurements are first performed with the pressure vessel in a turbopumped vacuum state. After completion of vacuum measurements, in-gas measurements are taken on pairs of isotherms: seven pressures (105 kPa, 199 kPa, 300 kPa, 400 kPa, 499 kPa, 600 kPa and 700 kPa) on a p-rising isotherm, followed by the same pressures in reverse order on a p-falling isotherm.

When changing to a new pressure set point on a given isotherm, working gas is added or removed from the pressure vessel; two small vent ports in the resonator shell connect the gas space bounded by the resonator cavity inner surface with the pressure vessel gas space outside the resonator [12]. TM11 microwave mode resonance measurements are performed continuously throughout this process to monitor the state of the working gas inside the resonator and ensure that thermal and pressure equilibrium have been achieved before commencing main RIGT data collection at the new pressure.

At each pressure on each isotherm, main data collection consists of ten repeated microwave scans of each of five microwave modes (TM11, TE11, TM12, TE12, TM13). The burdensome procedure applied previously to extrapolate

results to zero heater power [12] is no longer needed, since the problematic heater has been disabled. Once the pair of isotherms has been completed, the pressure vessel is returned to a turbopumped vacuum state and further microwave measurements are performed.

2.4. Data analysis procedure

For each measured microwave resonance triplet scan, either $(T - T_{90})$ of the working gas or κ_T of the resonator cavity is calculated as follows:

(i) Using the average measured pressure p during the scan (corrected for static head effects), average measured T_{90} during the scan, and equation (6), the experimentally-measured refractive index of the working gas n_{expt} is determined.

(ii) A golden section search is performed to find the thermodynamic temperature T that minimizes $\left|n_{\text{expt}}^2 - n_{\text{calc}}^2\right|$, where the theoretically-calculated refractive index of the working gas n_{calc} is obtained from equations (1)–(4).

(iii)

  (A) If the scan was performed at TPXe, the average T_{90} measured during the scan is subtracted from T to obtain $(T - T_{90})$.
  (B) If the scan was performed at TPW, an additional larger golden section search encompassing steps (i) and (ii) is performed to find the value of κ_T such that $T = T_{90}$.

The mean and standard deviation of the resulting one hundred $(T - T_{90})$ or κ_T values are calculated for each pressure set point on the combined pair of isotherms (ten microwave scans of each of five microwave modes on each of two isotherms). The 'hybrid' analysis approach proposed in [6] is then applied to determine a final $(T - T_{90})$ or κ_T result for the given pair of
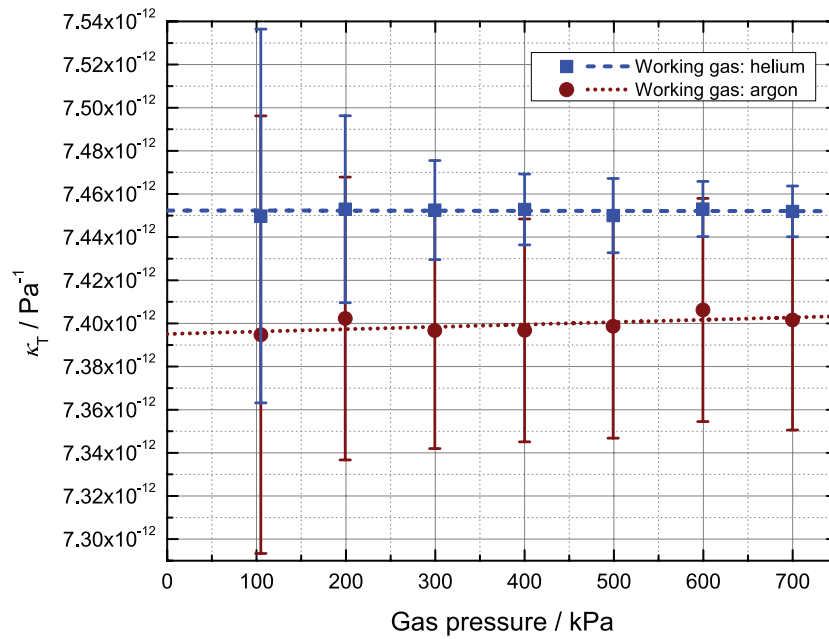
Figure 3. Measured κ_T versus p at TPW, analyzed using vacuum data collected after each pair of isotherms. Data points and uncertainty bars are respectively the means and standard deviations of the results from 100 microwave scans performed at each measurement pressure on each pair of isotherms. Dashed and dotted lines are linear fits to the data, inversely weighted by the squares of the standard deviations.

isotherms by fitting the mean values to a linear function of p and extrapolating to $p = 0$ (the inverse squares of the standard deviations are used to weight the fit).

In some cases, a characteristic low-pressure upturn or downturn is seen in the $(T - T_{90})$ or κ_T isotherm data, dependent on the particular vacuum data set used to determine $a_{0,m}$ but manifesting consistently for all microwave modes on a given pair of isotherms, indicating a disagreement between the measurements made in vacuum relative with those made at higher pressures. This effect was eliminated by replacing $a_{0,m}$ in equation (6) with $(a_{0,m} + \Delta a_0)$, where Δa_0 is a mode-independent, pressure-independent correction applied identically to both isotherms in a given pair. In the present study, Δa_0 was observed to be either positive, negative or zero, with absolute magnitudes on the order of the lattice constant of face-centred cubic copper (0.36 nm at 293 K [32]). All measurements at TPW and TPXe are plotted below after application of the Δa_0 correction, with final results calculated by taking into account $(a_{0,m} + \Delta a_0)$ from the vacuum measurements performed both before and after each pair of isotherms.

3. Measurement of the effective isothermal compressibility of the resonant cavity at the triple point of water

3.1. Measurements and analysis with helium as working gas

Microwave measurements with helium as the working gas were performed at TPW according to section 2.3 and analyzed to determine κ_T according to section 2.4. The *ab initio* calculated properties of helium used in the analysis largely follow the advice given in [6]: A_ϵ from Puchalski *et al* [33], A_μ from Bruch and Weinhold [6, 34–36], B_ϵ from Rizzo *et al* [37], C_ϵ

from Heller and Gelbart [12, 38], B_ρ from Cencek *et al* [39], C_ρ from Garberoglio *et al* [40], and D_ρ from Shaul *et al* [41]. Virial coefficients of higher order than these were set to zero, such that equations (2)–(4) were truncated as in [12].

The resulting pressure-dependent κ_T data and linear fit are shown in figure 3 for the case calculated using post-isotherm vacuum data. Combining the fit results from pre- and post-isotherm vacuum cases yields an average $p = 0$ intercept of $\kappa_T = 7.452\,398 \times 10^{-12}$ Pa^{-1}, with an average fitting uncertainty of 1.8×10^{-15} Pa^{-1}. The difference between the $p = 0$ intercepts for the two cases is 8.2×10^{-17} Pa^{-1}.

3.2. Measurements and analysis with argon as working gas

Microwave measurements with argon as the working gas were also performed at TPW according to section 2.3 and analyzed to determine κ_T according to section 2.4. As with helium, above, the *ab initio* calculated and experimentally-derived properties of argon used in the analysis are mostly based on the recommendations of [6]: A_ϵ from Gaiser and Fellmuth [28], A_μ from Barter *et al* [6, 42], B_ϵ from Vogel *et al* [43], C_ϵ from a linear fit to the argon data of Huot and Bose [44] (with the fit inversely weighted by the squares of the uncertainties of each data point), B_ρ from Gaiser and Fellmuth [29], C_ρ from Cencek *et al* [45], and D_ρ from the average of the values of Wiebke *et al* and Jäger *et al* [6, 46, 47]. As above, virial coefficients of higher order than these were set to zero, such that equations (2)–(4) were truncated as in [12].

The resulting pressure-dependent κ_T data and linear fit are shown in figure 3 for the case calculated using post-isotherm vacuum data. Combining the fit results from pre- and post-isotherm vacuum cases yields an average $p = 0$ intercept of $\kappa_T = 7.395\,153 \times 10^{-12}$ Pa^{-1}, with an average fitting

Table 2. Standard uncertainty of the TPW κ_T determination.

	Working gas: helium (Pa^{-1})	Working gas: argon (Pa^{-1})	Correlation
Uncertainty components, Type B			
T of TPW	3.8×10^{-16}	3.0×10^{-15}	1
p measurement	5.4×10^{-15}	4.3×10^{-14}	1
p static head	8.1×10^{-16}	6.5×10^{-14}	1
A_ϵ impurities	4.9×10^{-15}	4.4×10^{-14}	0
A_ϵ literature	1.2×10^{-16}	2.0×10^{-14}	0
A_μ literature	7.5×10^{-18}	1.2×10^{-15}	0
Higher virial coefficients	3.5×10^{-17}	2.4×10^{-15}	0
a_0	4.1×10^{-17}	4.8×10^{-17}	0
Resonator thermal gradient	1.5×10^{-15}	4.3×10^{-15}	0
TPW realization	3.8×10^{-16}	3.0×10^{-15}	1
CSPRT self-heating	2.1×10^{-16}	1.7×10^{-15}	1
Uncertainty component, Type A			
Extrapolation to zero pressure	1.8×10^{-15}	3.8×10^{-15}	0
Combined standard uncertainty	7.7×10^{-15}	9.2×10^{-14}	
Measured κ_T value	$7.4524(77) \times 10^{-12}$	$7.395(92) \times 10^{-12}$	
Measured κ_T weighted mean	$7.4540(72) \times 10^{-12}$		
OFHC Cu κ_T literature value [12, 32]	$7.45(11) \times 10^{-12}$		

uncertainty of 3.8×10^{-15} Pa^{-1}. The difference between the $p = 0$ intercepts for the two cases is 9.6×10^{-17} Pa^{-1}.

3.3. Uncertainty budget

The uncertainty budget for the κ_T determination at TPW is given in table 2, including correlations. Since the data analysis procedure to obtain κ_T described in section 2.4 relies on the identity $T = T_{90}$ at TPW, many of the uncertainty components in table 2 have been calculated first in terms of temperature equivalents that would shift T or T_{90} away from satisfying that identity. The temperature-equivalents are then converted into uncertainties on the compressibility (listed in table 2) by applying the absolute value of the sensitivity factor relating the $p = 0$ intercept of the linear κ_T fit to changes in the assumed value of $(T - T_{90})$. For helium, this sensitivity factor is -3.75×10^{-15} Pa^{-1}mK^{-1}, whereas for argon it is -3.00×10^{-14} Pa^{-1}mK^{-1}. The absolute value of the sensitivity factor for argon is $8\times$ larger than that for helium, due to argon's $8\times$ larger polarizability: when using RIGT to measure the compressibility of a resonator according to equation (5) and figure 1, best results are obtained when the frequency shift due to cavity compression is maximized relative to the frequency shift due to microwave refraction, so the enhanced polarizability of argon is counterproductive in this application.

Due to the recent re-definition of the kelvin to be based on a fixed value of the Boltzmann constant rather than a fixed value of the thermodynamic temperature of TPW, T of TPW now has a 0.1 mK uncertainty [19]. Averaged over the set of pressures used in the present study, the piston gauge pressure measurement relative uncertainty is 5.3 ppm in pressure, which corresponds to 1.45 mK at TPW, dominated by the

calibration uncertainty in the area of the piston. The pressure measurement uncertainty contribution is the largest component in the uncertainty budget for the κ_T determination using helium as the working gas.

The difference in static head of the working gas between the measuring plane of the piston gauge and the equator of the resonator is handled as in [12], amounting to a correction of 0.03(79) ppm in pressure for helium at TPW and 0.40(7.97) ppm in pressure for argon at TPW, which correspond to temperature-equivalent uncertainties of 0.217 mK and 2.18 mK respectively. Note that the static head correction and its uncertainty is $10\times$ larger for argon than for helium due to argon's $10\times$ larger mass density; when converted into compressibility-equivalents, the static head uncertainty contribution becomes $80\times$ larger for argon than for helium, and is the largest component in the uncertainty budget for the κ_T determination using argon as the working gas.

No correction or uncertainty component due to the thermomolecular effect is applied, since this effect is vanishingly small for the RIGT measurements performed thus far at NRC: by evaluating equation (3) from [48] using the smallest interior tube radius present in the gas line linking the room-temperature gas-handling system to the pressure vessel (1.59 mm) and lowest gas pressure used in the data analysis at each isotherm temperature, the worst case thermomolecular effect is estimated as in terms of pressure as 0.005 ppm at TPW, 0.02 ppm at TPXe, 0.03 ppm at TPAr, and 0.05 ppm at TPO$_2$ and TPNe.

Uncertainty contributions due to the unfiltered gas impurities listed in table 1 are estimated via the effect on A_ϵ as in [12]. For helium, this uncertainty, dominated by the detection limit for xenon impurities, is 4.75 ppm on A_ϵ which is

equivalent to 1.30 mK at TPW. For argon, this uncertainty, dominated by the detection limit for neon impurities, is 5.37 ppm on A_ϵ which is equivalent to 1.47 mK at TPW.

The uncertainty in the literature value of A_ϵ for helium [33] is equivalent to 0.032 mK at TPW, while that for argon [28] is equivalent to 0.66 mK at TPW. Similarly, the uncertainty in the literature value of A_μ relative to the literature value of A_ϵ for helium [6, 33–36] corresponds to 0.002 mK at TPW, whereas that for argon [6, 28, 42] corresponds to 0.040 mK at TPW.

One advantage of extrapolating the isotherm data to $p = 0$ via the 'hybrid' analysis method described in section 2.4 is that it reduces the reliance of the results on the values of the higher virial coefficients [6]. The uncertainty component due to higher virial coefficients characterizes the residual influence of the uncertainties in, and alternate literature sources of, the higher virials on the $p = 0$ intercept of the linear κ_T fit. For helium, this component is dominated by the large uncertainty ascribed to C_ϵ [12], with a minor contribution characterizing the effects of using an alternative B_ϵ from Moszynski *et al* [49] in place of that from Rizzo *et al* [37]. For argon, this component is dominated by the contribution characterizing the effects of using an alternative B_ρ from Mehl in Supplement B of Moldover *et al* [4] in place of that from Gaiser and Fellmuth [29].

The uncertainty contribution due to all aspects of the measurement of the vacuum radius of the resonating cavity $a_{0,m}$ and the efficacy of the Δa_0 correction thereof (section 2.4) is estimated as half of the difference between the $p = 0$ κ_T intercepts obtained from two cases with independently measured $a_{0,m}$ data sets and Δa_0 corrections: the analyses respectively using the pre- and post-isotherm vacuum measurements (sections 3.1 and 3.2).

Higher working gas pressures in the gas line connecting the pressure vessel to the room-temperature gas-handling system serve to enhance the thermal link along this pathway and induce a static vertical thermal gradient across the resonator shell, with the top of the resonator (strongly coupled through solid copper to cooling stage 2 of the cryocooler) colder than the bottom. Microwave resonance measurements average over the entire volume of gas inside the resonating cavity, including any thermal gradients thereof, so the uncertainty in the average T_{90} of the resonator due to thermal gradients is conservatively estimated using a rectangular distribution applied to half of the temperature difference exhibited between the two CSPRTs mounted on the resonator at 700 kPa, where the gradient is strongest. For helium, the total gradient across the resonator during isotherm measurements rose monotonically from 0.631 mK at 105 kPa to 1.415 mK at 700 kPa, leading to an uncertainty component on the average T_{90} of $1.415 \text{ mK}/(2\sqrt{3}) = 0.408$ mK. For argon, the total gradient across the resonator during isotherm measurements rose monotonically from 0.136 mK at 105 kPa to 0.495 mK at 700 kPa, leading to an uncertainty component on the average T_{90} of $0.495 \text{ mK}/(2\sqrt{3}) = 0.143$ mK.

The standard TPW realization uncertainty for CSPRTs calibrated at NRC on the ITS-90 is 0.1 mK. Furthermore, the uncertainty in the self-heating correction applied to the T_{90}

readings of CSPRT R4794 at TPW was 0.050 mK, and the uncertainty in the self-heating correction applied to the T_{90} readings of CSPRT 1876687 at TPW was 0.100 mK, propagating into an uncertainty component of 0.056 mK on the self-heating corrected resonator T_{90} averaged over the readings of both thermometers.

The 'hybrid' approach described in section 2.4 for the analysis of isotherm data is significantly streamlined compared to the previous NRC RIGT study [12], and intrinsically subsumes many Type A uncertainty components that were overcounted in the prior publication by being evaluated separately. The fitting uncertainty on the linear fit $p = 0$ intercept (from section 3.1 for helium and section 3.2 for argon) is now taken as the overall Type A uncertainty in the κ_T determination for each working gas.

The combined standard uncertainty for the RIGT κ_T measurement at TPW is 7.7×10^{-15} Pa^{-1} when helium is used as the working gas and 9.2×10^{-14} Pa^{-1} when argon is used as the working gas.

3.4. Weighted mean value

Combining the $7.4524(77) \times 10^{-12}$ Pa^{-1} κ_T value measured at TPW using helium with the $7.395(92) \times 10^{-12}$ Pa^{-1} κ_T value measured at TPW using argon, and taking into account correlations, gives a final weighted mean value for the compressibility of the particular resonator artifact used in the present study of $\kappa_T = 7.4540(72) \times 10^{-12}$ Pa^{-1} at TPW. The weighted mean value falling outside the interval bounded by the two input values is a consequence of the correlated part of the uncertainty being larger than the uncorrelated part while having different sensitivities for the measurements using helium and argon. This final experimentally-determined κ_T value is consistent with that calculated from equation (7) using the literature data sources discussed in [12] for the properties of OFHC copper (mostly drawn from [32]), but with considerably smaller uncertainty.

4. Extrapolation of the effective isothermal compressibility of the resonant cavity to lower temperatures

4.1. Extrapolation to the triple points of xenon, argon, oxygen and neon

In order to apply the experimentally-determined κ_T from section 3 to the analysis of microwave measurements at TPXe and below, it is extrapolated to temperatures lower than TPW following the prescription of Gaiser and Fellmuth [27]. Since the extrapolation is performed in terms of the adiabatic compressibility κ_S, the measured κ_T is first converted to κ_S by subtracting $\Delta_{S \to T}$ at TPW, then extrapolated according to equation (8), then converted from κ_S back to κ_T by adding $\Delta_{S \to T}$ at the temperature of interest. In all cases, the values and uncertainties of $\Delta_{S \to T}$ are calculated via the second term of equation (7), using the OFHC copper literature sources for α_L, c_p and ρ_{solid} summarized in [12, 25]. Previous microwave measurements showed that the present resonator's thermal

Table 3. Standard uncertainties of the extrapolated κ_T values.

	TPXe (Pa^{-1})	TPAr (Pa^{-1})	TPO$_2$ (Pa^{-1})	TPNe (Pa^{-1})
Uncertainty components, Type B				
Propagated from measurements at TPW	8.6×10^{-15}	8.6×10^{-15}	8.5×10^{-15}	8.5×10^{-15}
'Mono' versus 'poly'	7.2×10^{-15}	1.1×10^{-14}	1.2×10^{-14}	1.2×10^{-14}
Internal consistency of 'mono'	1.8×10^{-16}	2.9×10^{-15}	7.4×10^{-15}	1.4×10^{-14}
Internal consistency of 'poly'	3.8×10^{-15}	1.5×10^{-14}	2.3×10^{-14}	2.7×10^{-14}
Adiabatic to isothermal conversion	2.7×10^{-15}	1.1×10^{-15}	6.3×10^{-16}	1.3×10^{-16}
Combined standard uncertainty	1.2×10^{-14}	2.1×10^{-14}	2.8×10^{-14}	3.4×10^{-14}
Extrapolated measured κ_T value	$7.227(12) \times 10^{-12}$	$7.093(21) \times 10^{-12}$	$7.058(28) \times 10^{-12}$	$7.044(34) \times 10^{-12}$
OFHC Cu κ_T literature value [12, 32]	$7.21(10) \times 10^{-12}$	$7.09(10) \times 10^{-12}$	$7.06(10) \times 10^{-12}$	$7.04(10) \times 10^{-12}$

expansion is consistent with the literature for copper [25], and the specific heat of metals is relatively insensitive to processing [6]. At TPW, $\Delta_{S \to T} = 1.926(50) \times 10^{-13}$ Pa^{-1}, so $\kappa_T = 7.4540(72) \times 10^{-12}$ Pa^{-1} from section 3 corresponds to $\kappa_S = 7.2614(88) \times 10^{-12}$ Pa^{-1}.

Temperature-dependent compressibility measurements near TPW do not exist for the resonator used in the present study, so the Anderson–Grüneisen parameter δ appearing in equation (8) is drawn from two experimental literature data sets for OFHC copper: measurements of monocrystalline copper samples reported by Overton and Gaffney ('mono') [50], and measurements of polycrystalline copper samples reported by Ledbetter ('poly') [51]. In each case, δ is calculated as a function of temperature from the published data using α_L from [32] (with fit coefficients corrected as in [25]), and then averaged over a temperature region spanning several tens of kelvin near TPW in which δ is temperature independent [27]. For the data of Overton and Gaffney, an average value of $\delta_{mono} = 3.28$ is obtained over a temperature-independent region spanning from 145 K to 295 K. For the data of Ledbetter, an average value of $\delta_{poly} = 3.67$ is obtained over a temperature-independent region spanning from 265 K to 295 K.

Although the microwave resonator used in the present study is constructed of polycrystalline copper rather than monocrystalline copper, its measured $\kappa_S = 7.2614 \times 10^{-12}$ Pa^{-1} is closer to the Overton and Gaffney 'mono' $\kappa_S = 7.2624 \times 10^{-12}$ Pa^{-1} than the Ledbetter 'poly' $\kappa_S = 7.1759 \times 10^{-12}$ Pa^{-1} at TPW. Since further information to decide between the 'mono' and 'poly' data sets is lacking, the extrapolation is performed separately using both δ_{mono} and δ_{poly} and then averaged together.

Starting from $\kappa_S = 7.2614(88) \times 10^{-12}$ Pa^{-1} at TPW, at TPXe the adiabatic compressibility extrapolated using δ_{mono} is $\kappa_{S,mono} = 7.1386 \times 10^{-12}$ Pa^{-1}, and that extrapolated using δ_{poly} is $\kappa_{S,poly} = 7.1242 \times 10^{-12}$ Pa^{-1}, giving an average $\kappa_S = 7.1314 \times 10^{-12}$ Pa^{-1}. $\Delta_{S \to T} = 9.52(27) \times 10^{-14}$ Pa^{-1} at TPXe, so $\kappa_T = 7.2266 \times 10^{-12}$ Pa^{-1}.

At TPAr, $\kappa_{S,mono} = 7.0737 \times 10^{-12}$ Pa^{-1}, and $\kappa_{S,poly} = 7.0517 \times 10^{-12}$ Pa^{-1}, giving an average $\kappa_S = 7.0627 \times 10^{-12}$ Pa^{-1}. $\Delta_{S \to T} = 3.00(11) \times 10^{-14}$ Pa^{-1} at TPAr, so $\kappa_T = 7.0927 \times 10^{-12}$ Pa^{-1}.

At TPO$_2$, $\kappa_{S,mono} = 7.0598 \times 10^{-12}$ Pa^{-1}, and $\kappa_{S,poly} = 7.0362 \times 10^{-12}$ Pa^{-1}, giving an average $\kappa_S = 7.0480 \times 10^{-12}$ Pa^{-1}. $\Delta_{S \to T} = 9.7(6) \times 10^{-15}$ Pa^{-1} at TPO$_2$, so $\kappa_T = 7.0577 \times 10^{-12}$ Pa^{-1}.

At TPNe, $\kappa_{S,mono} = 7.0551 \times 10^{-12}$ Pa^{-1}, and $\kappa_{S,poly} = 7.0310 \times 10^{-12}$ Pa^{-1}, giving an average $\kappa_S = 7.0431 \times 10^{-12}$ Pa^{-1}. $\Delta_{S \to T} = 5(1) \times 10^{-16}$ Pa^{-1} at TPNe, so $\kappa_T = 7.0436 \times 10^{-12}$ Pa^{-1}.

4.2. Uncertainty budget

The uncertainty budget for the κ_T extrapolation is given in table 3.

The uncertainty in the TPW value of κ_S (8.8×10^{-15} Pa^{-1}) is propagated to the lower temperatures of interest by replacing $\kappa_S(\text{TPW})$ in equation (8) with its uncertainty, and averaging over δ_{mono} and δ_{poly}.

An uncertainty component characterizing the disagreement between the 'mono' and 'poly' extrapolations is calculated as half of the absolute value of the difference between $\kappa_{S,mono}$ and $\kappa_{S,poly}$.

The internal consistency of the 'mono' extrapolation case is assessed as the difference between the literature value of κ_S from Overton and Gaffney at the temperature of interest [50] and that extrapolated to the same temperature from Overton and Gaffney's TPW κ_S value, using $\delta_{mono} = 3.28$ and equation (8). Similarly, the internal consistency of the 'poly' extrapolation case is assessed as the difference between the literature value of κ_S from Ledbetter at the temperature of interest [51] and that extrapolated to the same temperature from Ledbetter's TPW κ_S value, using $\delta_{poly} = 3.67$ and equation (8). As the temperature is decreased and Ledbetter's measured κ_S values deviate further from those found in the small temperature-independent region near TPW, the uncertainty contribution due to the internal consistency of the 'poly' extrapolation comes to dominate the uncertainty budget.

Lastly, there is an uncertainty contribution due to the uncertainty in the adiabatic to isothermal compressibility conversion $\Delta_{S \to T}$ at the temperature of interest.

The combined standard uncertainties in the extrapolated κ_T values increase by roughly a factor of three from 1.2×10^{-14}
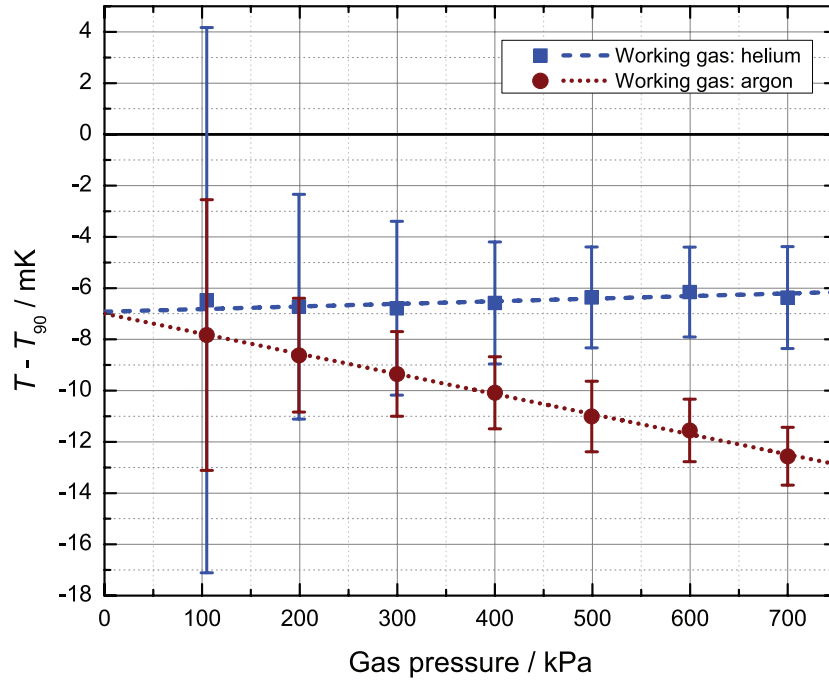
Figure 4. Measured $(T - T_{90})$ versus p at TPXe, analyzed using vacuum data collected after each pair of isotherms. Data points and uncertainty bars are respectively the means and standard deviations of the results from 100 microwave scans performed at each measurement pressure on each pair of isotherms. Dashed and dotted lines are linear fits to the data, inversely weighted by the squares of the standard deviations.

Pa^{-1} at TPXe to 3.4×10^{-14} Pa^{-1} at TPNe, due to the reduced internal consistency of the 'poly' extrapolation as temperature is lowered.

4.3. Final extrapolated values

Including uncertainty, the final isothermal compressibilities extrapolated from the *in situ* measurement of the resonator compressibility at TPW are: $\kappa_{\mathrm{T}} = 7.227(12) \times 10^{-12}$ Pa^{-1} at TPXe, $\kappa_{\mathrm{T}} = 7.093(21) \times 10^{-12}$ Pa^{-1} at TPAr, $\kappa_{\mathrm{T}} = 7.058(28) \times 10^{-12}$ Pa^{-1} at TPO$_2$, and $\kappa_{\mathrm{T}} = 7.044$ $(34) \times 10^{-12}$ Pa^{-1} at TPNe. These values are consistent with those calculated from equation (7) using the literature data sources discussed in [12] for the properties of OFHC copper (mostly drawn from [32]), but with uncertainties between 3× and 8× smaller.

5. Measurement of the thermodynamic temperature of the triple point of xenon

5.1. Measurements and analysis with helium as working gas

Microwave measurements with helium as the working gas were performed at TPXe according to section 2.3, and analyzed to determine $(T - T_{90})$ according to section 2.4, using $\kappa_{\mathrm{T}} = 7.227(12) \times 10^{-12}$ Pa^{-1} from section 4. Literature sources of the *ab initio* calculated properties of helium used in this analysis are the same as in section 3.1.

The resulting pressure-dependent $(T - T_{90})$ data and linear fit are shown in figure 4 for the case calculated using post-isotherm vacuum data. Combining the fit results from pre- and

post-isotherm vacuum cases yields an average $p = 0$ intercept of $(T - T_{90}) = -6.923$ mK, with an average fitting uncertainty of 0.22 mK. The difference between the $p = 0$ intercepts for the two cases is 0.006 mK.

5.2. Measurements and analysis with argon as working gas

Microwave measurements with argon as the working gas were also performed at TPXe according to section 2.3, and analyzed to determine $(T - T_{90})$ according to section 2.4, using $\kappa_{\mathrm{T}} = 7.227(12) \times 10^{-12}$ Pa^{-1} from section 4. Literature sources of the *ab initio* calculated and experimentally-derived properties of argon used in this analysis are the same as in section 3.2, with two exceptions: B_ρ was measured by Gaiser and Fellmuth only at TPW [29] so is replaced at TPXe with B_ρ from Jäger *et al* [47], and C_ρ is only listed by Cencek *et al* at a few sparse temperatures near TPXe [45] so is replaced there with C_ρ from Jäger *et al* [47].

The resulting pressure-dependent $(T - T_{90})$ data and linear fit are shown in figure 4 for the case calculated using post-isotherm vacuum data. Combining the fit results from pre- and post-isotherm vacuum cases yields an average $p = 0$ intercept of $(T - T_{90}) = -6.951$ mK, with an average fitting uncertainty of 0.13 mK. The difference between the $p = 0$ intercepts for the two cases is 0.084 mK.

5.3. Uncertainty budget

The uncertainty budget for the $(T - T_{90})$ determination at TPXe is given in table 4, including correlations. The sources of uncertainty comprising the uncertainty budget, along with

Table 4. Standard uncertainty of the TPXe $(T - T_{90})$ determination.

	Working gas: helium (mK)	Working gas: argon (mK)	Correlation
T uncertainty components, Type B			
κ_T	1.1	0.14	1
p measurement	0.86	0.86	1
p static head	0.21	2.3	1
A_ϵ impurities	0.76	0.87	0
A_ϵ literature	0.019	0.39	0
A_μ literature	0.001	0.023	0
Higher virial coefficients	0.014	0.16	0
a_0	0.003	0.042	0
T_{90} uncertainty components, Type B			
Resonator thermal gradient	0.63	0.31	0
TPW realization	0.050	0.050	1
Propagated calibration uncertainty	0.29	0.29	1
Type 1 non-uniqueness (SRI)	0.074	0.074	1
Type 3 non-uniqueness (NU3)	0.14	0.14	1
CSPRT self-heating	0.056	0.056	1
$(T - T_{90})$ uncertainty component, Type A			
Extrapolation to zero pressure	0.22	0.13	0
$(T - T_{90})$ combined standard uncertainty	1.8	2.7	
$(T - T_{90})$ value	−6.9(1.8)	−7.0(2.7)	
$(T - T_{90})$ weighted mean	−6.9(1.7)		

the approaches used to estimate them, are largely the same as already described in section 3.3. However, unlike in section 3, at TPXe a known κ_T value (from section 4) is used to obtain T, rather than using a known T to obtain κ_T, so the uncertainty component due to the uncertainty in the knowledge of T of TPW is replaced with a component due to the uncertainty in the knowledge of κ_T at TPXe. For helium, the sensitivity factor relating the $p = 0$ intercept of the linear $(T - T_{90})$ fit to changes in the value of κ_T is -9.31×10^{13} mK Pa, whereas for argon it is -1.16×10^{13} mK Pa. The absolute value of the sensitivity factor for argon is $8\times$ smaller than that for helium, due to argon's $8\times$ larger polarizability: when using RIGT to measure the thermodynamic temperature according to equation (5) and figure 1, best results are obtained when the frequency shift due to microwave refraction is maximized relative to the frequency shift due to cavity compression, so the enhanced polarizability of argon is helpful in this application. Applying the absolute values of these sensitivity factors to the 1.2×10^{-14} Pa^{-1} uncertainty in the TPXe-extrapolated experimental value of κ_T from table 3 gives uncertainty contributions on T of 1.1 mK for helium and 0.14 mK for argon.

This is the largest component in the uncertainty budget for the $(T - T_{90})$ determination using helium as the working gas.

The piston gauge pressure measurement relative uncertainty of 5.3 ppm in pressure corresponds to 0.86 mK at TPXe. The static pressure head correction is 4.3(1.3) ppm in pressure for helium at TPXe and 45(14) ppm in pressure for argon at TPXe, which correspond to temperature-equivalent uncertainties of 0.21 mK and 2.3 mK respectively. As in section 3.3, the static head correction and its uncertainty is approximately $10\times$ larger for argon than for helium due to argon's $10\times$ larger mass density; this is the largest component in the uncertainty budget for the $(T - T_{90})$ determination using argon as the working gas, and it is responsible for the poorer overall uncertainty of the argon $(T - T_{90})$ determination than that of helium, despite argon's lower sensitivity to resonator compressibility.

For helium, the uncertainty contribution due to the unfiltered gas impurities of 4.75 ppm on A_ϵ is equivalent to 0.76 mK at TPXe. For argon, the gas impurity uncertainty contribution of 5.37 ppm on A_ϵ is equivalent to 0.87 mK at TPXe.

The uncertainty in the literature value of A_ϵ for helium [33] is equivalent to 0.019 mK at TPXe, while that for argon [28] is equivalent to 0.39 mK at TPXe. Similarly, the uncertainty in the literature value of A_μ relative to the literature value of A_ϵ for helium [6, 33–36] corresponds to 0.001 mK at TPXe, whereas that for argon [6, 28, 42] corresponds to 0.023 mK at TPXe.

For helium, as in section 3.3, the residual uncertainty component due to higher virial coefficients is dominated by the large uncertainty ascribed to C_ϵ [12] (the contribution characterizing the effects of using an alternative B_ϵ from Moszynski et al [49] in place of that from Rizzo et al [37] is less than 1 µK for the data at TPXe). For argon, this component is dominated by the contributions characterizing the effects of using an alternative B_ρ from Mehl in Supplement B of Moldover et al [4] in place of that from Jäger et al [47], and using the alternative C_ρ from Cencek et al (applying spline interpolations to the sparse value and uncertainty table) [45] in place of that from Jäger et al [47], with minor contributions due to the uncertainties in B_ϵ [43] and C_ϵ [44].

As in section 3.3, the uncertainty contribution due to all aspects of the measurement of the vacuum radius of the resonating cavity $a_{0,m}$ and the efficacy of the Δa_0 correction thereof (section 2.4) is estimated as half of the difference between the $p = 0$ $(T - T_{90})$ intercepts obtained from two cases with independently measured $a_{0,m}$ data sets and Δa_0 corrections: the analyses respectively using the pre- and post-isotherm vacuum measurements (sections 5.1 and 5.2).

As in section 3.3, the uncertainty in the average T_{90} of the resonator due to thermal gradients is estimated using a rectangular distribution applied to half of the temperature difference exhibited between the two CSPRTs mounted on the resonator at 700 kPa, where the gradient is strongest. For helium, the total gradient across the resonator during isotherm measurements rose monotonically from 0.28 mK at 105 kPa to 2.19 mK at 700 kPa, leading to an uncertainty component on the average T_{90} of 2.19 mK$/(2\sqrt{3}) = 0.63$ mK. For argon, the total gradient across the resonator during isotherm
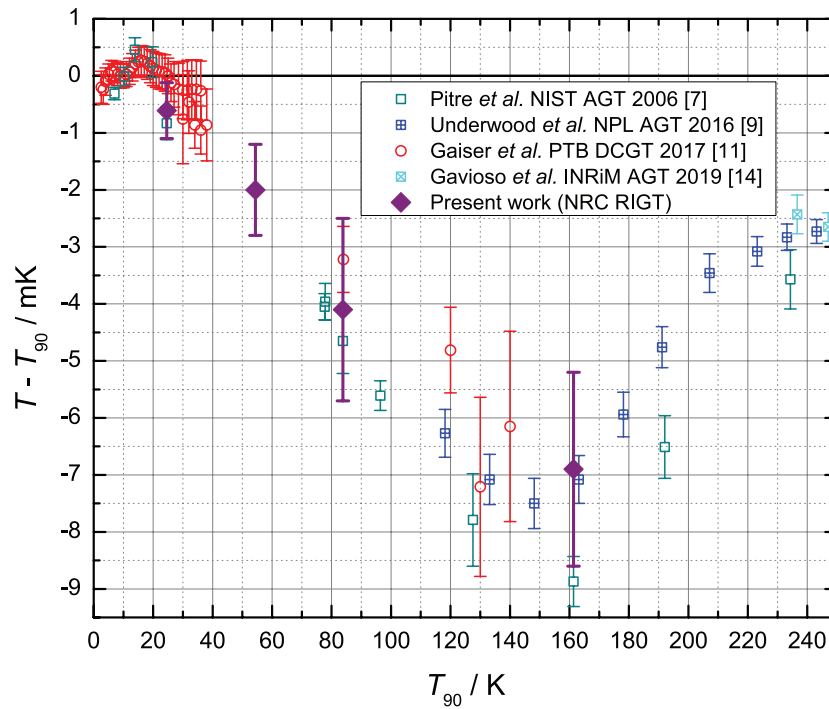
Figure 5. NRC RIGT ($T - T_{90}$) results from the present study compared to measurements made using other primary thermometry techniques of acoustic gas thermometry (AGT) [7, 9, 14] and dielectric constant gas thermometry (DCGT) [11].

measurements rose monotonically from 0.20 mK at 105 kPa to 1.09 mK at 700 kPa, leading to an uncertainty component on the average T_{90} of 1.09 mK/$(2\sqrt{3})$ = 0.31 mK.

The standard TPW realization uncertainty for CSPRTs calibrated at NRC on the ITS-90 is 0.1 mK, which becomes 0.050 mK when propagated to TPXe [22]. Since, unlike TPW, TPXe is not currently a defining fixed point for thermometer calibrations on the ITS-90, additional T_{90} uncertainty components must be included due to: uncertainties of the calibration points propagated to the temperature of interest, Type 1 non-uniqueness ('subrange inconsistency' or 'SRI'), and Type 3 non-uniqueness ('NU3'). At TPXe, these are respectively 0.29 mK [22], 0.074 mK [52], and 0.14 mK [52]. The uncertainties in the self-heating corrections of both CSPRTs were the same at TPXe as at TPW.

As in section 3.3, the fitting uncertainty on the linear fit $p = 0$ intercept (from section 5.1 for helium and section 5.2 for argon) is taken as the overall Type A uncertainty in the $(T - T_{90})$ determination for each working gas.

The combined standard uncertainty for the RIGT $(T - T_{90})$ measurement at TPXe is 1.8 mK when helium is used as the working gas and 2.7 mK when argon is used as the working gas.

5.4. Weighted mean value

Combining the $-6.9(1.8)$ mK $(T - T_{90})$ value measured at TPXe using helium with the $-7.0(2.7)$ mK $(T - T_{90})$ value measured at TPXe using argon, and taking into account correlations, gives a final weighted mean value for the thermodynamic accuracy of the ITS-90 in the present study of $(T - T_{90}) = -6.9(1.7)$ mK measured by RIGT at TPXe.

Since the uncertainty budget shown in table 4 is dominated by uncertainty components on T rather than T_{90}, and is considerably larger than the uncertainty in $T_{90} = 161.405\,96(32)$ K of TPXe [22], the results of the present study determine the thermodynamic temperature of the triple point of xenon to be $T = (161.3991 \pm 0.0017)$ K.

6. Re-calculation of the thermodynamic accuracy of the ITS-90 at the triple points of argon, oxygen and neon

Since the previous NRC RIGT measurements [12] used the same quasi-spherical resonator artifact as in the present study, the new experimentally-measured compressibility of this resonator can be used to re-calculate $(T - T_{90})$ at TPAr ($T_{90} = 83.8058$ K), TPO2 ($T_{90} = 54.3584$ K), and TPNe ($T_{90} = 24.5561$ K). Limitations in the previous experimental set-up mean that the streamlined data analysis and uncertainty budget approach of the present work cannot be applied to the old data, so the $(T - T_{90})$ values and uncertainties are re-calculated using the analysis methods of [12], while making only two narrow changes:

(i) The literature-derived κ_T values and uncertainties are replaced with those determined experimentally in section 3 and extrapolated to low temperatures in section 4.

(ii) The value of the molar gas constant R has been updated as per the new fixed values of the Avogadro and Boltzmann constants [18, 19]. Removing its associated uncertainty component from the T uncertainty budgets reduces the combined standard uncertainties of T by 0.001 mK or less at all three temperatures.

Using the new $\kappa_T = 7.093(21) \times 10^{-12}$ Pa^{-1} value and uncertainty at TPAr reduces the $(T - T_{90})$ value by 0.025 mK, reduces the Type B T uncertainty component due to κ_T to 0.5 mK, reduces the combined standard uncertainty of T to 1.4 mK, and reduces the $(T - T_{90})$ combined standard uncertainty to 1.6 mK. Using the new R value at TPAr reduces the $(T - T_{90})$ value by 0.028 mK. Altogether, the revised thermodynamic accuracy of the ITS-90 measured by NRC RIGT is $(T - T_{90}) = -4.1(1.6)$ mK at TPAr.

Using the new $\kappa_T = 7.058(28) \times 10^{-12}$ Pa^{-1} value and uncertainty at TPO$_2$ increases the $(T - T_{90})$ value by 0.022 mK, reduces the Type B T uncertainty component due to κ_T to 0.3 mK, reduces the combined standard uncertainty of T to 0.7 mK, and reduces the $(T - T_{90})$ combined standard uncertainty to 0.8 mK. Using the new R value at TPO$_2$ reduces the $(T - T_{90})$ value by 0.018 mK. Altogether, the revised thermodynamic accuracy of the ITS-90 measured by NRC RIGT is $(T - T_{90}) = -2.0(8)$ mK at TPO$_2$.

Using the new $\kappa_T = 7.044(34) \times 10^{-12}$ Pa^{-1} value and uncertainty at TPNe leaves the $(T - T_{90})$ value unchanged, reduces the Type B T uncertainty component due to κ_T to 0.07 mK, reduces the combined standard uncertainty of T to 0.43 mK, and reduces the $(T - T_{90})$ combined standard uncertainty to 0.49 mK. Using the new R value at TPNe reduces the $(T - T_{90})$ value by 0.008 mK. Altogether, the revised thermodynamic accuracy of the ITS-90 measured by NRC RIGT is $(T - T_{90}) = -0.61(49)$ mK at TPNe.

These revised $(T - T_{90})$ values and uncertainties replace those published in [12].

7. Conclusion

Refractive index gas thermometry has been performed at NRC with helium and argon as working gases. Microwave resonance measurements have been taken at the triple points of water ($T = T_{90} = 273.16$ K) and xenon ($T_{90} = 161.405\,96$ K). The measurements at the triple point of water were used to experimentally determine the isothermal compressibility of the resonating cavity, which was then extrapolated to the triple points of xenon, argon ($T_{90} = 83.8058$ K), oxygen ($T_{90} = 54.3584$ K), and neon ($T_{90} = 24.5561$ K). The extrapolated compressibilities agree with those from the OFHC copper literature, but with uncertainties three to eight times smaller.

Applying the extrapolated compressibility and a new 'hybrid' data analysis method to the microwave measurements at the triple point of xenon reveals the thermodynamic temperature $T = 161.3991(17)$ K and thermodynamic accuracy of the ITS-90 $(T - T_{90}) = -6.9(1.7)$ mK at $T_{90} = 161.405\,96$ K.

The extrapolated compressibilities were also used to re-calculate the results of a previous NRC RIGT study at the temperatures of the triple points of argon, oxygen and neon, replacing the previously published results with new values and uncertainties of the thermodynamic accuracy of the ITS-90: $(T - T_{90}) = -4.1(1.6)$ mK at $T_{90} = 83.8058$ K,

$(T - T_{90}) = -2.0(8)$ mK at $T_{90} = 54.3584$ K, and $(T - T_{90}) = -0.61(49)$ mK at $T_{90} = 24.5561$ K.

Collectively, these results represent the first application of microwave resonator-based refractive index gas thermometry (RIGT) from the triple point of xenon to the triple point of neon. They are plotted in figure 5 and agree well with literature measurements made using other primary thermometry techniques of acoustic gas thermometry (AGT) and dielectric constant gas thermometry (DCGT).

ORCID iDs

P M C Rourke ⬤ https://orcid.org/0000-0001-7875-9592

References

[1] Preston-Thomas H 1990 The international temperature scale of 1990 (ITS-90) *Metrologia* **27** 3–10
[2] Preston-Thomas H 1990 The international temperature scale of 1990 (ITS-90) *Metrologia* **27** 107 (erratum)
[3] Rusby R L, Hudson R P, Durieux M, Schooley J F, Steur P P M and Swenson C A 1991 Thermodynamic basis of the ITS-90 *Metrologia* **28** 9–18
[4] Moldover M R, Gavioso R M, Mehl J B, Pitre L, de Podesta M and Zhang J T 2014 Acoustic gas thermometry *Metrologia* **51** R1–19
[5] Gaiser C, Zandt T and Fellmuth B 2015 Dielectric-constant gas thermometry *Metrologia* **52** S217–26
[6] Rourke P M C, Gaiser C, Gao B, Madonna Ripa D, Moldover M R, Pitre L and Underwood R J 2019 Refractive-index gas thermometry *Metrologia* **56** 032001
[7] Pitre L, Moldover M R and Tew W L 2006 Acoustic thermometry: new results from 273 K to 77 K and progress towards 4 K *Metrologia* **43** 142–62
[8] Fischer J, de Podesta M, Hill K D, Moldover M, Pitre L, Rusby R, Steur P, Tamura O, White R and Wolber L 2011 Present estimates of the differences between thermodynamic temperatures and the ITS-90 *Int. J. Thermophys.* **32** 12–25
[9] Underwood R, de Podesta M, Sutton G, Stanger L, Rusby R, Harris P, Morantz P and Machin G 2016 Estimates of the difference between thermodynamic temperature and the international temperature scale of 1990 in the range 118 K–303 K *Phil. Trans. R. Soc.* A **374** 20150048
[10] Underwood R, de Podesta M, Sutton G, Stanger L, Rusby R, Harris P, Morantz P and Machin G 2017 Further estimates of $(T - T_{90})$ close to the triple point of water *Int. J. Thermophys.* **38** 44

[11] Gaiser C, Fellmuth B and Haft N 2017 Primary thermometry from 2.5 K to 140 K applying dielectric-constant gas thermometry *Metrologia* **54** 141–7

[12] Rourke P M C 2017 NRC microwave refractive index gas thermometry implementation between 24.5 K and 84 K *Int. J. Thermophys.* **38** 107

[13] Cui J, Feng X J, Lin H, Zhang J T and Huan K W 2018 Thermodynamic temperature measurement using single cylindrical microwave resonator *Jiliang Xuebao/Acta Metrol. Sin.* **39** 255–61

[14] Gavioso R M, Madonna Ripa D, Steur P P M, Dematteis R and Imbraguglio D 2019 Determination of the thermodynamic temperature between 236 K and 430 K from speed of sound measurements in helium *Metrologia* **56** 045006

[15] Hill K D 2013 An evolutionary approach to updating the international temperature scale *AIP Conf. Proc.* **1552** 71–80

[16] Hill K D and Steele A G 2014 The international temperature scale: past, present, and future *NCSLI Measure J. Meas. Sci.* **9** 60–7

[17] Machin G 2018 The kelvin redefined *Meas. Sci. Technol.* **29** 022001

[18] Newell D B *et al* 2018 The CODATA 2017 values of h, e, k, and N_A for the revision of the SI *Metrologia* **55** L13–6

[19] Stock M, Davis R, de Mirandés E and Milton M J T 2019 The revision of the SI—the result of three decades of progress in metrology *Metrologia* **56** 022001

[20] BIPM consultative committee for thermometry 2019 *The International System of Units (SI brochure)* (*Appendix 2: Mise En Pratique for the Definition of the Kelvin in the SI*) 9th edn (Paris: BIPM) 20 May 2019 version (www.bipm. org/en/publications/mises-en-pratique/)

[21] UNEP 2013 Minamata convention on mercury: texts and annexes (UNEP Chemicals Branch, Geneva, Switzerland)

[22] Hill K D and Steele A G 2005 The triple point of xenon *Metrologia* **42** 278–88

[23] Steur P P M, Rourke P M C and Giraudi D 2019 Comparison of xenon triple point realizations *Metrologia* **56** 015008

[24] May E F, Pitre L, Mehl J B, Moldover M R and Schmidt J W 2004 Quasi-spherical cavity resonators for metrology based on the relative dielectric permittivity of gases *Rev. Sci. Instrum.* **75** 3307–17

[25] Rourke P M C and Hill K D 2015 Progress toward development of low-temperature microwave refractive index gas thermometry at NRC *Int. J. Thermophys.* **36** 205–28

[26] Schmidt J W, Gavioso R M, May E F and Moldover M R 2007 Polarizability of helium and gas metrology *Phys. Rev. Lett.* **98** 254504

[27] Gaiser C and Fellmuth B 2016 Method for extrapolating the compressibility data of solids from room to lower temperatures *Phys. Status Solidi* b **253** 1549–56

[28] Gaiser C and Fellmuth B 2018 Polarizability of helium, neon, and argon: new perspectives for gas metrology *Phys. Rev. Lett.* **120** 123203

[29] Gaiser C and Fellmuth B 2019 Highly-accurate density-virial-coefficient values for helium, neon and argon at 0.01 °C determined by dielectric-constant gas thermometry *J. Chem. Phys.* **150** 134303

[30] Rourke P M C 2016 The triple point of sulfur hexafluoride *Metrologia* **53** L1–L6

[31] SAES PS2-GC50-R specifications 2019 document S110-282_A, DCN 5793

[32] Simon N J, Drexler E S and Reed R P 1992 *Properties of Copper and Copper Alloys at Cryogenic Temperatures* (*National Institute of Standards Technology Monograph* vol 177) (Washington, DC: U.S. Government Printing Office) pp 1–850

[33] Puchalski M, Piszczatowski K, Komasa J, Jeziorski B and Szalewicz K 2016 Theoretical determination of the polarizability dispersion and the refractive index of helium *Phys. Rev.* A **93** 032515

[34] Bruch L W and Weinhold F 2000 Diamagnetism of helium *J. Chem. Phys.* **113** 8667–70

[35] Bruch L W and Weinhold F 2002 Nuclear motion and Breit–Pauli corrections to the diamagnetism of atomic helium *J. Chem. Phys.* **117** 3243–7

[36] Bruch L W and Weinhold F 2003 Nuclear motion and Breit–Pauli corrections to the diamagnetism of atomic helium *J. Chem. Phys.* **119** 638 (erratum)

[37] Rizzo A, Hättig C, Fernández B and Koch H 2002 The effect of intermolecular interactions on the electric properties of helium and argon. III. Quantum statistical calculations of the dielectric second virial coefficients *J. Chem. Phys.* **117** 2609–18

[38] Heller D F and Gelbart W M 1974 Short range electronic distortion and the density dependent dielectric function of simple gases *Chem. Phys. Lett.* **27** 359–64

[39] Cencek W, Przybytek M, Komasa J, Mehl J B, Jeziorski B and Szalewicz K 2012 Effects of adiabatic, relativistic, and quantum electrodynamics interactions on the pair potential and thermophysical properties of helium *J. Chem. Phys.* **136** 224303

[40] Garberoglio G, Moldover M R and Harvey A H 2011 Improved first-principles calculation of the third virial coefficient of helium *J. Res. Natl Inst. Stand. Technol.* **116** 729–42

[41] Shaul K R S, Schultz A J and Kofke D A 2012 Path-integral Mayer-sampling calculations of the quantum Boltzmann contribution to virial coefficients of helium-4 *J. Chem. Phys.* **137** 184101

[42] Barter C, Meisenheimer R G and Stevenson D P 1960 Diamagnetic susceptibilities of simple hydrocarbons and volatile hydrides *J. Phys. Chem.* **64** 1312–6

[43] Vogel E, Jäger B, Hellmann R and Bich E 2010 *Ab initio* pair potential energy curve for the argon atom pair and thermophysical properties for the dilute argon gas. II. Thermophysical properties for low-density argon *Mol. Phys.* **108** 3335–52

[44] Huot J and Bose T K 1991 Experimental determination of the dielectric virial coefficients of atomic gases as a function of temperature *J. Chem. Phys.* **95** 2683–7

[45] Cencek W, Garberoglio G, Harvey A H, McLinden M O and Szalewicz K 2013 Three-body nonadditive potential for argon with estimated uncertainties and third virial coefficient *J. Phys. Chem.* A **117** 7542–52

[46] Wiebke J, Schwerdtfeger P, Moyano G E and Pahl E 2011 An atomistic fourth-order virial equation of state for argon from first principles calculations *Chem. Phys. Lett.* **514** 164–7

[47] Jäger B, Hellmann R, Bich E and Vogel E 2011 *Ab initio* virial equation of state for argon using a new nonadditive three-body potential *J. Chem. Phys.* **135** 084308

[48] Fellmuth B, Engert J, Shimazaki T and Sparasci F 2018 *Guide to the Realization of the ITS-90, Chapter 3: Vapour Pressure Scales and Pressure Measurements* (Paris: BIPM) 1 January 2018 version (www.bipm.org/en/committees/cc/cct/guide-its90.html)

[49] Moszynski R, Heijmen T G A and van der Avoird A 1995 Second dielectric virial coefficient of helium gas: quantum-statistical calculations from an *ab initio* interaction-induced polarizability *Chem. Phys. Lett.* **247** 440–6

[50] Overton W C and Gaffney J 1955 Temperature variation of the elastic constants of cubic elements. I. Copper *Phys. Rev.* **98** 969–77

[51] Ledbetter H M 1981 Elastic constants of polycrystalline copper at low temperatures *Phys. Status Solidi* A **66** 477–84

[52] Pokhodun A I, Fellmuth B, Pearce J V, Rusby R L, Steur P P M, Tamura O, Tew W L and White D R 2018 *Guide to the Realization of the ITS-90, Chapter 5: Platinum Resistance Thermometry* (Paris: BIPM 1 January 2018 version (www.bipm.org/en/committees/cc/cct/guide-its90.html)